V. 120, NO. 6
NOVEMBER 2023

ACI STRUCTURAL JOURNAL

A JOURNAL OF THE AMERICAN CONCRETE INSTITUTE

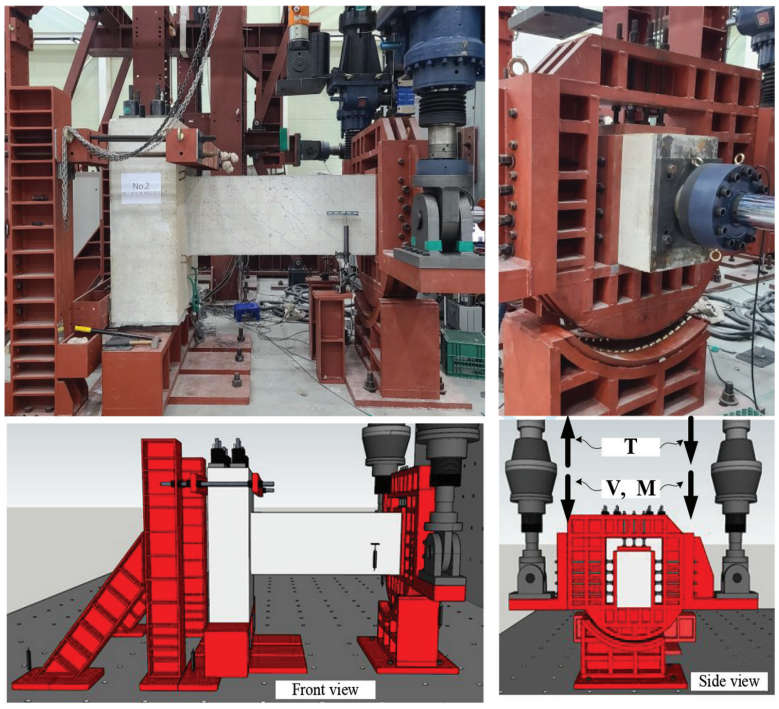

American Concrete Institute

ACI STRUCTURAL JOURNAL TECHNICAL PAPER

Title No. 120-S90

Strut-and-Tie Models Using Multi-Material and Multi-Volume Topology Optimization: Load Path Approach

by Tuo Zhao, Ammar A. Alshannaq, David W. Scott, and Glaucio H. Paulino

The development of strut-and-tie models (STMs) for the design of reinforced concrete (RC) deep beams considering a general multi-material and multi-volume topology optimization framework is presented. The general framework provides flexibility to control the location/inclination/length scale of the ties according to practical design requirements. Optimality conditions are applied to evaluate the performance of the optimized STM layouts. Specifically, the Michell number Z (or load path) is used as a simple and effective criterion to quantify the STMs. The experimental results confirm that the layout with the lowest load path Z achieves the highest ultimate load. Moreover, significantly reduced cracking is observed in the optimized layouts compared to the traditional layout. This observation implies that the optimized layouts may require less crack-control reinforcement, which would lower the total volume of steel required for the deep beams.

Keywords: load path; Michell number; multi-material topology optimization; reinforced concrete (RC) deep beam; strut and tie.

INTRODUCTION

In 1904, Michell wrote the revolutionary paper "The Limits of Economy of Material in Frame-Structures," which is a landmark in the field of optimization in general and topology optimization in particular. He derived the well-known Michell's optimality conditions (Michell 1904), that provide analytical ways to find optimal truss structures. The definition of the optimal structure is the least-weight truss with given allowable stresses, which is also known as the minimal total load path theory. The load path has been quantified using the Michell number, Z, defined as follows

$$Z = \sum_e |F_e| L_e = \sum_{e \in G^T} |F_e| L_e + \sum_{e \in G^C} |F_e| L_e \tag{1}$$

where L_e and F_e denote the length and internal axial force of the e-th truss member in the structure, respectively; and G^T and G^C are the sets of tension and compression members, respectively. For any statically determinate truss that is fully stressed (to the tensile stress limit σ^T and compressive stress limit σ^C), the volume of the truss can be calculated as follows

$$V = \frac{\sum_{e \in G^T} |F_e| L_e}{\sigma^T} + \frac{\sum_{e \in G^C} |F_e| L_e}{\sigma^C} = \frac{(\sigma^C + \sigma^T) Z + (\sigma^C - \sigma^T) C}{2 \sigma^C \sigma^T} \tag{2}$$

where $C = \sum_{e \in G^T} |F_e| L_e - \sum_{e \in G^C} |F_e| L_e$, which is known as the Maxwell number. Maxwell (1864) states that C is a constant value for given boundary and loading conditions—that is, C is independent of the structural layout. As a result, minimizing the load path Z for a given design problem is equivalent to minimizing the volume V if the structure is fully stressed.

A pioneering work by Kumar (1978) applies the load path theory of truss frameworks to design reinforced concrete (RC) deep beams by navigating optimal load transmission. Following and building upon Kumar's study, this work extends Michell's optimality conditions to understand the optimal load path for STMs and uses the load path Z (or the Michell number) as a criterion to quantify the efficiency of the STM. Compared to existing criteria (Schlaich et al. 1987; Xia et al. 2020; He et al. 2020), the present criterion is simpler. The experimental results in the "Load-deflection curves" section in this paper verify that the STM layout with the lowest load path Z (or Michell number) achieves the highest ultimate load.

The STMs are powerful tools for analyzing and designing RC structures. However, traditional STMs dramatically simplify the complex stress state found in deep concrete elements in compression, which greatly limits their efficiency in many practical design applications. More recently, topology optimization has been used to automatically generate STMs, including the works of Liang et al. (2000, 2001), Leu et al. (2006), Bruggi (2010), Mozaffari et al. (2020), and Zhou and Wan (2021), which is just a small sample of references in the field. The optimized STM layouts provide deeper insight into the load paths in RC members and, ultimately, aid in more efficient structural designs. However, most topology optimization formulations for STMs use only a single material, assuming the struts and ties have the same linear behavior. Victoria et al. (2011) extend the single material optimization using a bilinear material model with different behaviors in compression and tension to represent the struts and ties, respectively. Gaynor et al. (2013) and Jewett and Carstensen (2019) consider different materials for the struts and ties, but most are typically restricted to a single volume constraint for both materials (that is, each material volume cannot be constrained separately). Thus, these models are limited in practical application. In many real-world RC structure design cases, restricting the location of reinforcement (ties) to certain regions while controlling

ACI Structural Journal, V. 120, No. 6, November 2023.
MS No. S-2020-408.R3, doi: 10.14359/51739089, received March 21, 2023, and reviewed under Institute publication policies.

the allowable angle of inclination or length scale of ties according to design requirements is essential.

The aforementioned limitations can be addressed by a general multi-material topology optimization approach, which efficiently accommodates an arbitrary number of materials and constraints (Zhang et al. 2018; Sanders et al. 2018). This general approach is applied to a novel STM framework using multi-material topology optimization with multiple volume constraints. The present framework allows the designer to adjust the ties' locations, inclinations, and scales based on practical design specifications.

RESEARCH SIGNIFICANCE

This work proposes a simple and efficient criterion (the Michell number Z in Eq. (1)) to quantify the efficiency of the topologically optimized STMs. It is shown that the optimized STM layouts with lower Z outperformed the traditional layout in terms of improving load-bearing capacity and ductility. The framework developed in this paper can form the benchmark of an efficient, general, and practical STM design method for RC structures.

MULTI-MATERIAL AND MULTI-VOLUME TOPOLOGY OPTIMIZATION FORMULATION FOR STRUT-AND-TIE MODELS

The design for an optimal STM layout consists of determining the cross-sectional areas of the truss members using the ground structure method (GSM) (for example, Dorn et al. [1964]). In this method, the design domain is discretized using a set of nodes that are interconnected by truss members to form an initial ground (that is, reference) structure (GS). Based on a tailored design update scheme, unnecessary members are gradually removed from the initial GS; the optimal STM design is then obtained. The topology optimization formulation for STMs using the GSM is given as

$$\min_{\boldsymbol{x}_1,\boldsymbol{x}_2} J(\boldsymbol{x}_1,\boldsymbol{x}_2) = \min_{\boldsymbol{x}_1,\boldsymbol{x}_2} -\Pi(\boldsymbol{x}_1,\boldsymbol{x}_2,\boldsymbol{u}(\boldsymbol{x}_1,\boldsymbol{x}_2))$$

$$\text{s.t.} \sum_{i\in G^j} \boldsymbol{L}_i^T\boldsymbol{x}_i - V_{max}^j \le 0, j = 1,\ldots, n, \text{ and } i = 1, 2 \quad (3)$$

$$\text{with } \boldsymbol{u}(\boldsymbol{x}_1, \boldsymbol{x}_2) = \arg\min_{\boldsymbol{u}} \Pi(\boldsymbol{x}_1, \boldsymbol{x}_2, \boldsymbol{u})$$

where $\boldsymbol{x}_1$ and $\boldsymbol{x}_2$ are the vectors of design variables (cross-sectional areas of the truss members) for struts (concrete) and ties (reinforcement), respectively, which can be constrained separately, and s.t. is subject to. The objective function J is the negative total potential energy of the system in equilibrium, and $\boldsymbol{u}$ is the displacement vector (state variable), which is obtained as the minimizer of the potential energy Π; thus, general nonlinear constitutive behavior can be incorporated (Sanders et al. 2020). The formulation (Eq. (3)) considers a total of n independent volume constraints and denotes G^j as the set of material indexes for the j-th volume constraint. The term $\boldsymbol{L}_i^T\boldsymbol{x}_1$ indicates the total volume associated with the design variable $\boldsymbol{x}_1$, with $\boldsymbol{L}_i$ being the length vector for the i-th material, and V_{max}^j is the allowable volume for the j-th volume constraint. The main feature of Eq. (3) is that it can efficiently handle a general setting of volume constraints. In particular, defining material subregions will allow the control of locations/inclination/length scale of the ties according to practical design requirements.

Design-variable update scheme to general volume constraints for STMs

An essential component of any topology optimization framework is a reliable and efficient design-variable update scheme. Zhang et al. (2018) formulated a general design-variable update scheme tailored for the multi-material topology optimization formulation that does not require a predefined candidate material sequence and can efficiently and effectively handle an arbitrary number of candidate materials and volume constraints. Inspired by this work, the current study derives a design-variable update scheme for the present strut-and-tie optimization formulation (Eq. (3)).

The derivation of the design-variable update scheme is based on sequential explicit, convex approximations. The objective function in the formulation (Eq. (3)) is approximated at optimization step k as a convex function constructed based on the objective function gradient (Christensen and Klarbring 2008; Groenwold and Etman 2008). Introducing a set of intervening variable vectors $\boldsymbol{y}_i(\boldsymbol{x}_i)$, the approximation of the objective function at the k-th optimization step is

$$J^k(\boldsymbol{x}_1,\boldsymbol{x}_2) = J(\boldsymbol{x}_1^k,\boldsymbol{x}_2^k) + \sum_{i=1}^{2}\left[\frac{\partial J}{\partial \boldsymbol{y}_i}(\boldsymbol{x}_1^k,\boldsymbol{x}_2^k)\right]^T\left[\boldsymbol{y}_i(\boldsymbol{x}_i) - \boldsymbol{y}_i(\boldsymbol{x}_i^k)\right] \quad (4)$$

where $\boldsymbol{x}_1^k, \boldsymbol{x}_2^k$ are the values of the design variables at optimization step k; and $\partial J/\partial \boldsymbol{y}_i$ is the gradient of J with respect to the intervening variable $\boldsymbol{y}_i$, which depends on the gradient of J with respect to $\boldsymbol{x}_i$. In the following, to simplify the notation, $\boldsymbol{b}_i$ denotes this gradient $\partial J/\partial \boldsymbol{y}_i$. Having defined the approximated objective J^k, a subproblem (by neglecting the constant terms in J^k) is formulated as

$$\min_{\boldsymbol{x}_1,\boldsymbol{x}_2} \sum_{i=1}^{2}[\boldsymbol{b}_i(\boldsymbol{x}_1^k,\boldsymbol{x}_2^k)]^T\boldsymbol{y}_i(\boldsymbol{x}_i)$$

$$\text{s.t.} \sum_{i\in G^j} \boldsymbol{L}_i^T\boldsymbol{x}_i - V_{max}^j \le 0, j = 1, \ldots, nc \quad (5)$$

$$x_{i,L}^{(e),k} \le x_i^{(e)} \le x_{i,U}^{(e),k}, \forall i \text{ and } e$$

where $x_{i,L}^{(e),k}$ and $x_{i,U}^{(e),k}$ are the lower and upper bounds for the design variable $x_i^{(e)}$ determined through a user-prescribed move limit. Introducing a set of Lagrange multipliers λ_j for each volume constraint, the Lagrangian of the previous subproblem is expressed as

$$L(\boldsymbol{x}_1, \boldsymbol{x}_2, \lambda_1,\ldots, \lambda_{nc}) = \sum_{j=1}^{nc}\left\{\sum_{i\in G^j}\left[\left[\boldsymbol{b}_i(\boldsymbol{x}_1^k,\boldsymbol{x}_2^k)\right]^T\boldsymbol{y}_i(\boldsymbol{x}_i) + \lambda_j\boldsymbol{L}_i^T\boldsymbol{x}_i\right] - \lambda_j V_{max}^j\right\} \quad (6)$$

The previous Lagrangian function has a clearly separable structure with respect to each volume constraint. This means that the minimizer of the Lagrangian with respect to $\boldsymbol{x}_i$, denoted as $\boldsymbol{x}_i^*$, can be expressed in the following form

$$x_i^{(e)*} = Q_i^{(e)}\left(\boldsymbol{x}_1^k, \boldsymbol{x}_2^k, \lambda_j\right), \forall i \in G^j \tag{7}$$

In other words, $\boldsymbol{x}_i^*$ only depends on the Lagrange multiplier of the volume constraint associated with $\boldsymbol{x}_i$. Plugging $\boldsymbol{x}_i^*$ back into the Lagrangian gives the dual objective function

$$D(\lambda_1, \ldots, \lambda_{nc}) = L(\boldsymbol{x}_1^*, \boldsymbol{x}_2^*, \lambda_1, \ldots, \lambda_{nc}) = \sum_{j=1}^{nc}\left\{\sum_{i \in G^j}\left[\left[\boldsymbol{b}_i\left(\boldsymbol{x}_1^k, \boldsymbol{x}_2^k\right)\right]^T \boldsymbol{y}_i\left(\boldsymbol{x}_i^*\right) + \lambda_j \boldsymbol{V}_i^T \boldsymbol{x}_i^*\right] - \lambda_j V_{max}^j\right\} \tag{8}$$

Because $\boldsymbol{x}_i^*$ only depends on λ_j if $i \in G^j$, it concludes that the dual objective function D also has a separable structure with respect to λ_j—namely, $D(\lambda_1, \ldots, \lambda_{nc}) = \sum_{j=1}^{nc} D^j(\lambda_j)$. As a result, the set of maximizing Lagrange multipliers $\lambda_1^*, \ldots, \lambda_{nc}^*$ can be computed by sequentially calculating the maximizing Lagrange multiplier λ_j^* for each $D^j(\lambda_j)$. The general formula of the updated design variable is then obtained

$$x_i^{(e),\,k+1} = Q_i^{(e)}\left(\boldsymbol{x}_1^k, \boldsymbol{x}_2^k, \lambda_j^*\right), \forall i \in G^j \tag{9}$$

Based on the previous formula, because the update of the design variable depends only on the Lagrange multiplier of its corresponding volume constraint, the design variables associated with each volume constraint can be updated independently. The present design-variable update scheme has been applied to the STM design example shown in the next section.

NUMERICAL EXAMPLES

A practical computational tool for STMs is developed to assist engineers in better understanding and designing RC structures using the present multi-material topology optimization framework. The new STM framework will provide engineers with the flexibility to specify the inclination/length scale of reinforcement and to control the tensile (tie) regions where reinforcement needs to be placed depending on design requirements through the use of multiple volume constraints.

A numerical study is conducted on the STMs for the two-dimensional (2-D) RC deep beam, as shown in Fig. 1(a). In this example, both struts and ties are modeled using truss elements with bilinear material models, as shown in Fig. 1(b). Five design scenarios are considered in this numerical example. In the first scenario, two materials share the entire domain (refer to Fig. 1(c)), and each material is associated with an individual volume constraint—that is, $V_{max}^j = 0.5V_{max}$, $j = 1, 2$. In the second and third scenarios, two materials share and split the domain (Fig. 1(e) and (g)), and the tie region is constrained within two-thirds and half of the entire domain, respectively. In the last two scenarios, struts and ties share and split the domain (Fig. 1(i) and (k)), and the allowable angle of inclination of ties is restricted to 90 degrees and 45 degrees, respectively. The optimized results for the five scenarios are shown in Fig. 1(d), (f), (h), (j), and (l). From the comparison of the results, varying specified tie regions/inclinations can significantly affect the STM and, in turn, the behavior of the resulting RC beam.

Besides specifying the tie regions/inclinations, the present STM design framework allows engineers to control the length scale of struts and ties either together or independently. Considering the length scale of STM designs is important from a practical point of view because the difficulties in the construction of the deep beam highly depend on the design of reinforcing bars in the STM. The length control approach in the present STM design framework is demonstrated using the deep beam example shown in Fig. 1. Without any restrictions on the length scale, the layouts of the initial ground structure for both struts and ties are shown in Fig. 1(c). The corresponding optimized STM design is shown in Fig. 1(d) (which is the same plot as the one in Fig. 2(a)). This design can be simplified by restricting the length of members in the initial ground structures for both the struts and ties. For instance, assuming that the minimum length scale is $\sqrt{2}$, the optimized design is obtained, as shown in Fig. 2(b), which has a simpler topology than the design shown in Fig. 2(a). Two alternative designs in Fig. 2(c) and (e) are obtained considering different minimum length scales of $\sqrt{5}$ and $\sqrt{10}$, respectively. Moreover, the length scale control can be applied to ties independently. For example, assuming that only ties are restricted to the minimum length scales, the optimized designs are achieved in Fig. 2(d) and (f). These two designs have different topologies than the ones in Fig. 2(c) and (e) accounting for length scale control for both struts and ties together. In summary, the flexible length control approach provides a variety of alternative STM configurations with different levels of complexity on the final topology.

The present STM framework generates a variety of optimized STM designs considering the specified tie regions, proper angles of inclination, and minimum length scale of the reinforcement. Furthermore, the efficiency of those alternative designs is investigated using the unified load path criterion in Eq. (1).

The design library in Fig. 3 collects alternative STM designs for a deep beam structure. Among those designs, Fig. 3(a) and (b) present conventional STM design layouts suggested by ACI 318-19 (ACI Committee 318 2019). The optimized designs with the present framework are shown in Fig. 3(a) to (l). As all the designs in Fig. 3 are statically determinate for the given boundary conditions, the internal forces in struts and ties can be easily calculated using static equilibrium conditions. Consequently, the load path Z for each design is determined using Eq. (1). As the load path Z decreases, the efficiency of the STM increases. For example, the standard ACI layout in Fig. 3(a) has a larger load path Z than the optimized layout in Fig. 3(k). The test results in the "Load-deflection curves" section demonstrate that the specimen with an optimized STM layout (Fig. 3(k)) can achieve a greater ultimate load than the specimen with the standard ACI layout for a given volume of tension reinforcement (Fig. 3(a)).

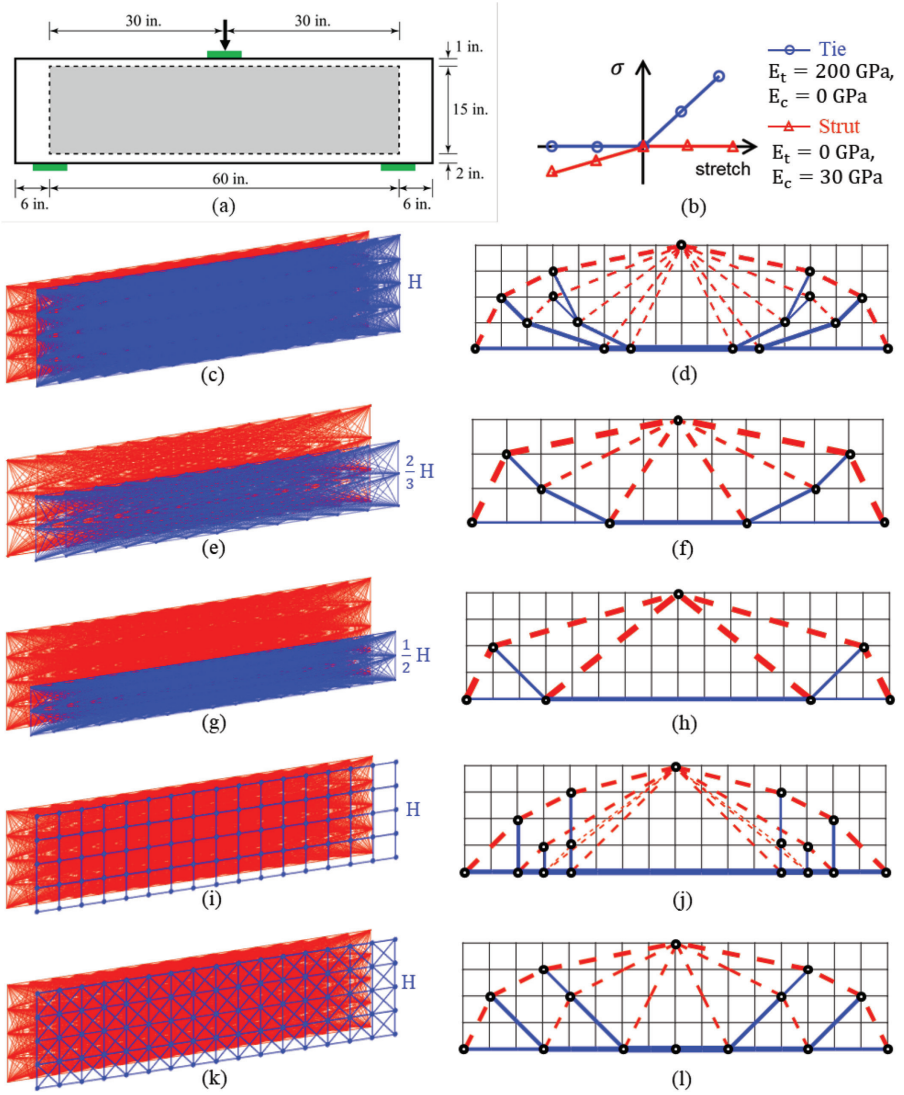

Fig. 1—Optimized strut-and-tie models for reinforced deep beam considering various design scenarios: (a) geometry of beam with highlighted design domain (that is, gray region); (b) simplified bilinear material model for both struts and ties; (c) scenario 1: strut (red) and tie (blue) regions share design domain; (d), (f), (h), (j), and (l) corresponding optimized STM designs for scenarios 1 to 5; (e) and (g) scenarios 2 and 3: tie region can only occupy two-thirds and half of entire domain, respectively; and (i) and (k) scenarios 4 and 5: allowable angle of inclination of tie is 90 degrees and 45 degrees, respectively. (Note: Full-color PDF of this paper can be accessed at www.concrete.org.)

EXPERIMENTAL EVALUATION OF OPTIMIZED STRUT-AND-TIE MODELS

The experimental research on RC deep beams presented in the literature focuses on the conventional STMs suggested by ACI 318 (Schlaich et al. 1987; MacGregor 1997; Breña and Roy 2009; Birrcher et al. 2009; Panjehpour et al. 2015; Ismail 2016; Ismail et al. 2018; Martinez et al. 2017; Rezaei et al. 2019; Kondalraj and Appa Rao 2021). The present work selects two optimized STMs (Fig. 4(b) and (c)) and compares their behavior with the most common STM (Fig. 4(a)) of ACI 318-19. The designs employed contained one significant deviation from ACI 318 guidelines: crack-control reinforcement (ACI 318-19, Section 23.5) was omitted from the beam designs to allow an evaluation of the relative crack pattern development in the various beams. Five RC deep beam specimens were constructed: two for the standard ACI model, one for optimized layout I, and two for optimized layout II. All five specimens have the same geometry as shown in Fig. 5. Regarding the reinforcement arrangements of the specimens, a longitudinal reinforcement ratio $\rho = 2\%$ was used for each specimen. To visualize the reinforcement layouts in a formwork, a three-dimensional (3-D) rendering of the reinforcement design was generated, as shown in Fig. 6(a) to (i), with more reinforcement details for the specimens given in Appendix A. Figures 6(h) and (i) show the designs involving multiple layers of reinforcing bars. Positioning those reinforcing bars inside formwork can be challenging from a construction perspective. To overcome this issue, customized reinforcing bar chairs were created using 3-D printing. Using this method, the geometry of the reinforcing bar chairs can be specified for a given reinforcement design. For example, the two customized reinforcing bar chairs in Fig. 7 facilitated the accurate positioning of the reinforcing bars.

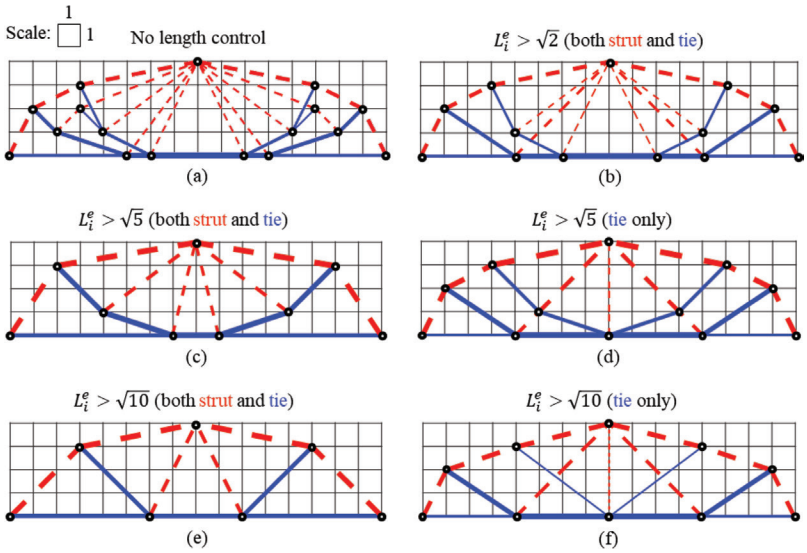

Fig. 2—Flexible length control for optimized STM (assuming that dimension of unit square in background grid for each design is 1): (a) optimized design without length constraints for both struts and ties; (b), (c), and (e) optimized designs with length constraints for both struts and ties, where upper bound of length is defined as √2, √5, and √10, respectively; and (d) and (f) optimized designs with length constraints on ties only, with allowable length defined as √5 and √10, respectively.

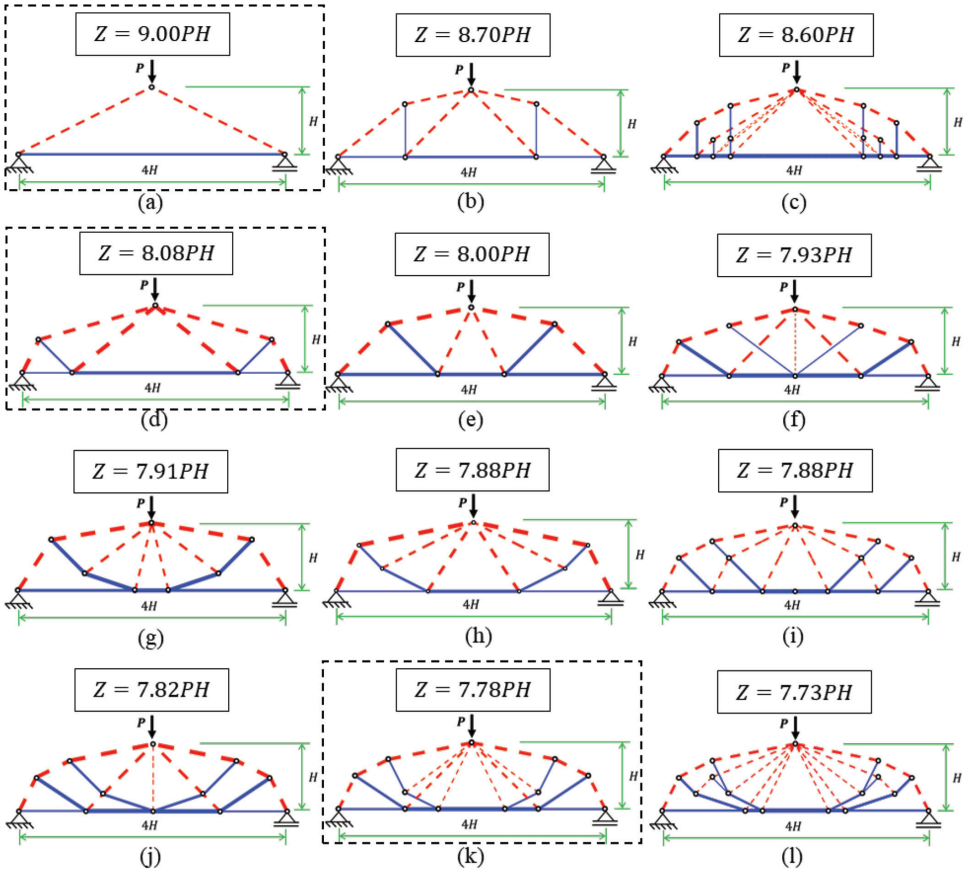

Fig. 3—Deep beam STM design library. Load path Z (that is, Eq. (1)) indicates efficiency of alternative designs in this library. As load path Z decreases through (a) to (l), efficiency of corresponding design improves. Three highlighted layouts (that is, (a), (d), and (k)) are selected for experimental validation in "Experimental Evaluation of Optimized Strut-and-Tie Models" section.

Experimental setup and procedure

The beams were cast with concrete having a compressive strength of 8.5 ksi (58.6 MPa) at the time of testing and reinforced with Grade 60 steel reinforcing bars (nominal yield strength of 60 ksi [414 MPa]). Reinforcing bar development was checked according to ACI 318-19; refer to Fig. 5 for visualizations of beam and support locations and Appendix A for reinforcement layouts. The steel reinforcing bars of the five RC deep beams were instrumented with 350 Ω strain gauges prior to concrete casting. The locations of the strain

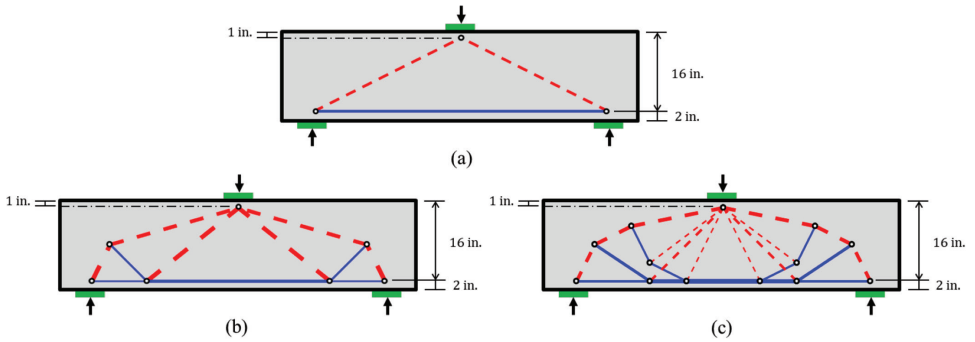

Fig. 4—Three layouts of strut-and-tie models for experimental evaluation: (a) conventional model in ACI 318-19; and (b) and (c) two optimized strut-and-tie models. (Note: 1 in. = 25.4 mm.)

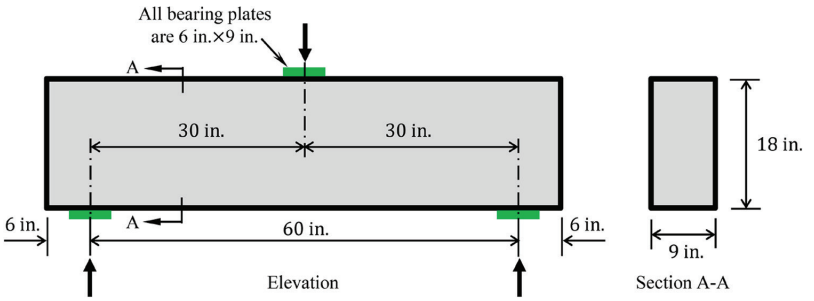

Fig. 5—Deep beam specimen geometry for evaluating optimized strut-and-tie models. (Note: 1 in. = 25.4 mm.)

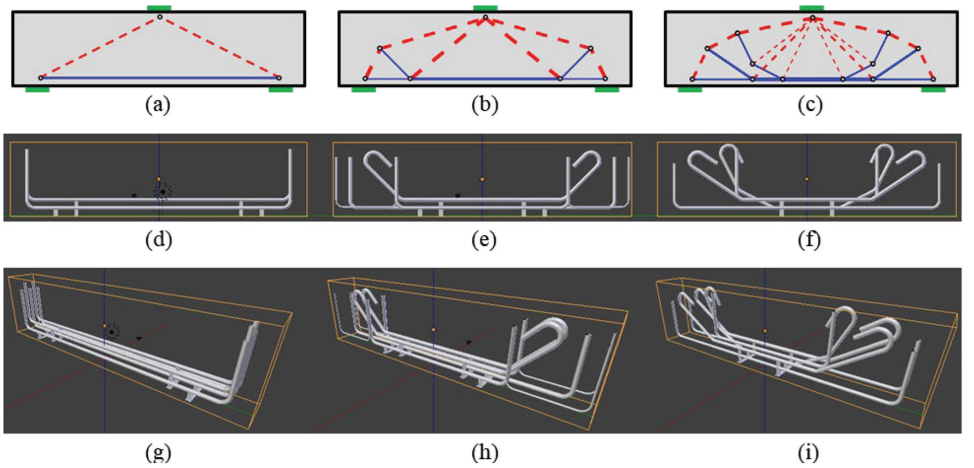

Fig. 6—Schematics of STM reinforcement layouts: (a) to (c) three selected STM layouts designated as standard ACI layout, optimized layout I, and optimized layout II, respectively; (d) to (f) front view of reinforcement designs; and (g) to (i) perspective view of reinforcement designs.

gauges were selected to monitor the role of key reinforcing bars in the optimized layouts; these locations are labeled in the three figures of Appendix A. Figures 8(a) to (c) show the steel reinforcement used for the tested beams of the ACI layout, optimized layout I, and optimized layout II, respectively. Also, the lead wires for the strain gauges are presented in Fig. 8. Moreover, two linear variable differential transformers (LVDTs) were used to estimate the effective strain in the concrete struts. For the midspan deflection, a string potentiometer was used. A 200 kip (890 kN) load cell connected to a hydraulic load ram was used to record load values. The test setup and instrumentation are shown in Fig. 9.

The program of testing consisted of applying an increasing load while monitoring crack initiation on the beam. Once a crack was visually observed, the hydraulic jack valve was closed to hold the load constant, and the cracks and their corresponding load values were highlighted on the beam. Additional load was then applied; this process was repeated until extensive cracks were observed, which prevented further safe monitoring. At that point, continuous loading to complete failure was carried out, and the failure load was recorded.

Load-deflection curves

An increasing load was applied to the specimen until it eventually failed. The load-deflection behavior of the

specimens is shown in Fig. 10 as solid/dashed curves. Each curve represents the applied load versus the midspan deflection of the deep beam. The ultimate loads (that is, maximum loads measured in the specimens) considering the three different STM layouts are given in Table 1. It is observed that the optimized STM layout II (Specimen No. 5), which has the lowest load path Z, reaches the highest ultimate load; and the standard ACI STM layout (Specimens No. 1 and 2), which has the largest load path Z, achieves the lowest ultimate load. This indicates that the load path Z can serve as an effective criterion to evaluate the efficiency of the STM.

Moreover, the initial stiffness values are observed to decrease with the optimization in the reinforcement design. This can be attributed to the fact that the optimized designs have more reinforcement closer to the cross section's neutral axis, which results in a smaller moment of area for transformed cross sections when determining the overall transformed cross-sectional stiffness.

Furthermore, deflection values are increased with optimized layouts I and II (Specimens No. 3 to 5) compared to the standard ACI layout (Specimens No. 1 and 2). This demonstrates the improved behavior of the optimized designs in which more tension cracks in the central region, more steel yielding, and, thus, more efficient load paths (Z) were observed.

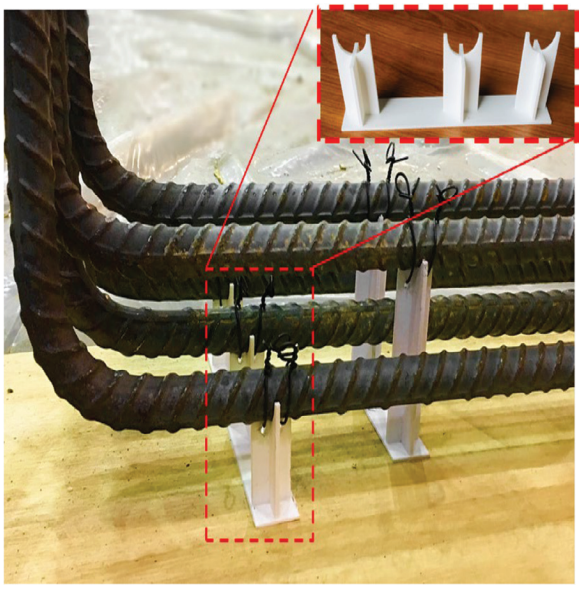

Fig. 7—Positioning reinforcement using 3-D-printed reinforcing bar chairs (fused filament fabrication, with polylactic acid [PLA] plastic material).

Observed failure modes

The failure modes of the specimens, considering the standard ACI STM layout (Specimens No. 1 and 2) and optimized layout I (Specimen No. 3), were characterized by strut

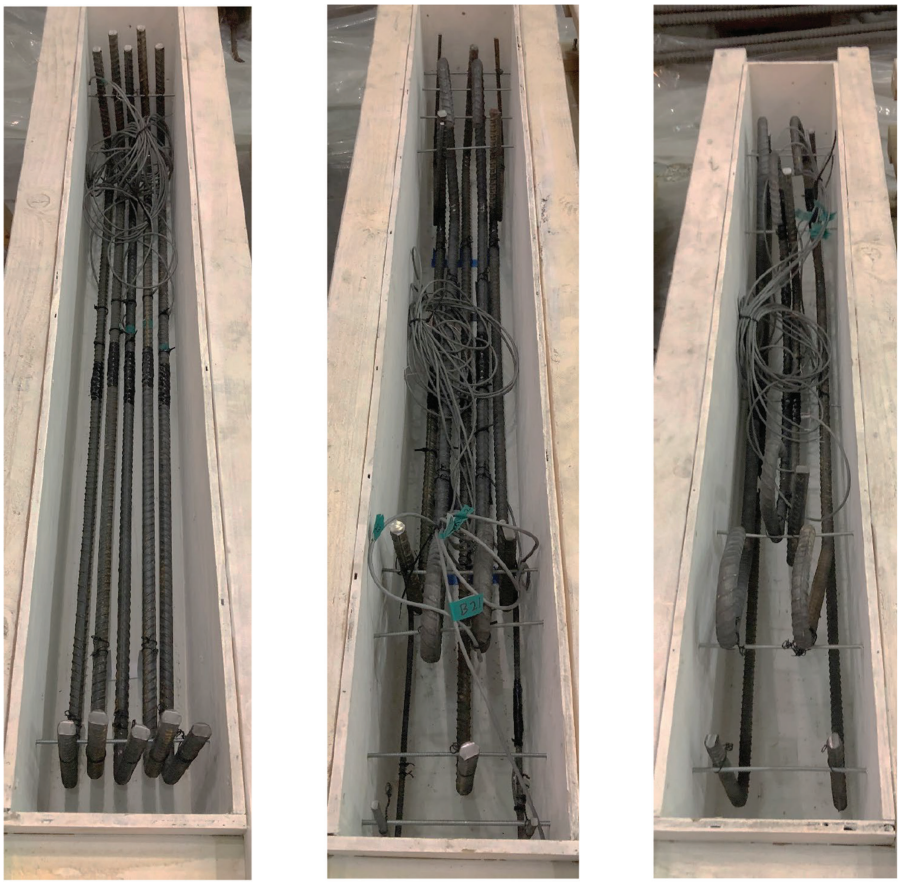

Fig. 8—Steel reinforcement cages used for: (a) ACI layout; (b) optimized layout I; and (c) optimized layout II.

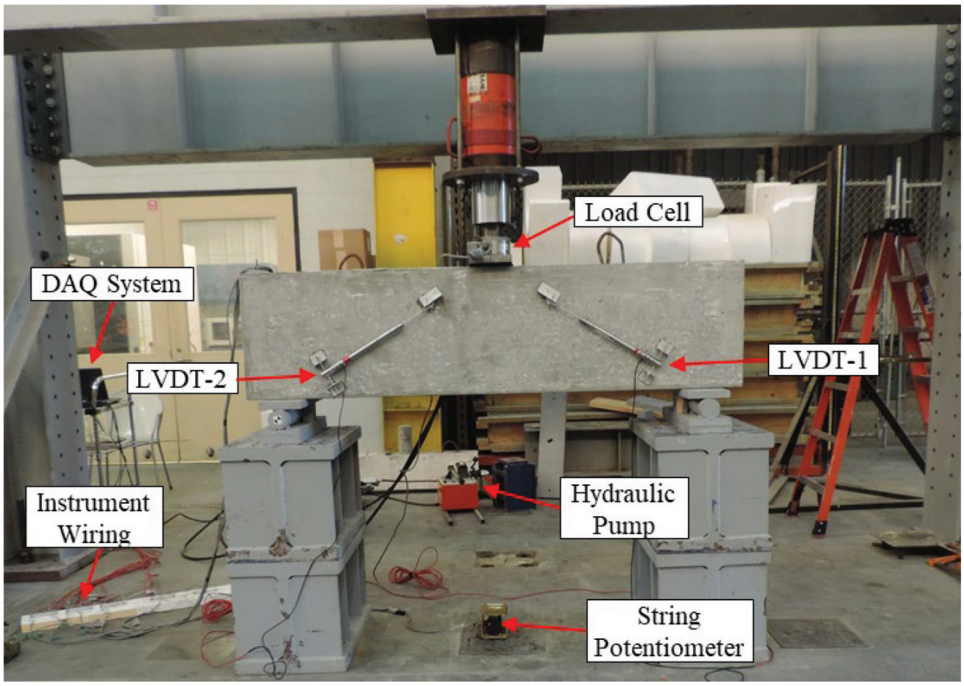

Fig. 9—Experimental setup and testing station.

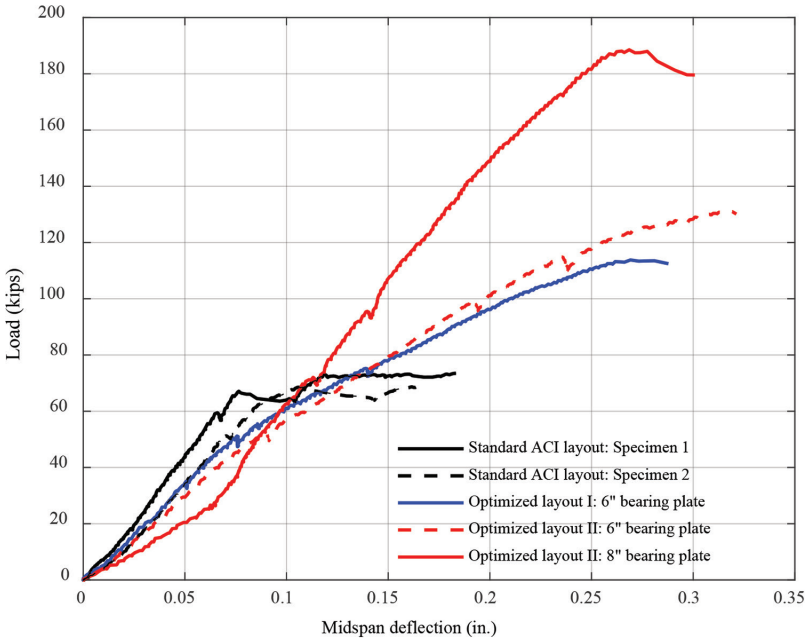

Fig. 10—Test results of deep beams considering different STM layouts. (Note: 1.0 in. = 25.4 mm; 1.0 kip = 4.45 kN.)

crushing. However, the ACI layout had larger crack widths compared to optimized layout I, which can be attributed to the more efficient load path *Z* introduced by more inclined steel reinforcing bars to mitigate large crack widths. On the other hand, the specimens with optimized STM layout II (Specimens No. 4 and 5) had a different failure mode characterized by bearing failure instead of strut failure, as shown in Fig. 11(f) and (h). When optimized layout II was tested with a 6 in. (0.15 m) bearing support plate (Specimen No. 4), the failure mode was characterized by bearing failure, showing the improved design obtained with more inclined steel reinforcing bars and a more optimal load path *Z*, which mitigates the inclined strut failure mode of the tested specimen. To attempt to avoid an undesirable experimental failure mode in the optimized layout II specimens, the bearing plate width was increased from 6 to 8 in. (0.15 to 0.20 m) for the load test of Specimen No. 5. A higher load capacity was observed using the 8 in. (0.20 m) bearing plates, even though the section still failed in bearing. This shift of the controlling failure mode (for optimized layout II) demonstrates the effectiveness of the novel STM layout. Future testing can incorporate more robust bearing layouts, which are expected to result in further optimization of the proposed STM.

Figure 11 shows how the total number of observed tension cracks (cracks in the midspan region of the beam) increased for optimized layouts I (Specimen No. 3) and II

with 6 in. (0.15 m) (Specimen No. 4) and 8 in. (0.20 m) (Specimen No. 5) bearing schemes. Moreover, shear cracks were observed to reduce in optimized layout I compared to the standard ACI design. No shear cracks were observed in optimized layout II (both 6 and 8 in. [0.15 and 0.20 m] bearing schemes). In terms of first crack loads in the struts, crack initiation was observed in the ACI layout (Specimens No. 1 and 2) at 66 kip (294 kN). Crack initiation for optimized layout I (Specimen No. 3) was observed at 75 kip (334 kN), and crack initiation for optimized layout II with a 6 in. (0.15 m) bearing (Specimen No. 4) was observed at 114 kip (507 kN). The strut crack initiation for optimized layout II with an 8 in. (0.20 m) bearing (Specimen No. 5) is not included in this discussion because the test was not halted for crack inspection after 94 kip (418 kN) for safety reasons; however, it can be reported that no cracks were observed up to the 94 kip (418 kN) load. These observations indicate a definable improvement in the load-carrying behavior for the optimized designs.

Table 1—Comparison of load path *Z* and ultimate load for three strut-and-tie layouts

STM layout	Load path (Eq. (1))	Specimen	Ultimate load, kip (kN)
Standard ACI	9.00*PH*	No. 1 (6 in. [0.15 m] bearing plate)	73.5 (327)
		No. 2 (6 in. [0.15 m] bearing plate)	68.7 (305)
Optimized I	8.08*PH*	No. 3 (6 in. [0.15 m] bearing plate)	114 (506)
Optimized II	7.78*PH*	No. 4 (6 in. [0.15 m] bearing plate)	131 (583)
		No. 5 (8 in. [0.20 m] bearing plate)	189 (839)

Observed strain gauge values

As discussed previously, strain gauges were used in specific locations on the internal reinforcement of the test specimens to attempt to compare the strain progression of the various reinforcement layouts under loading. Figure 12

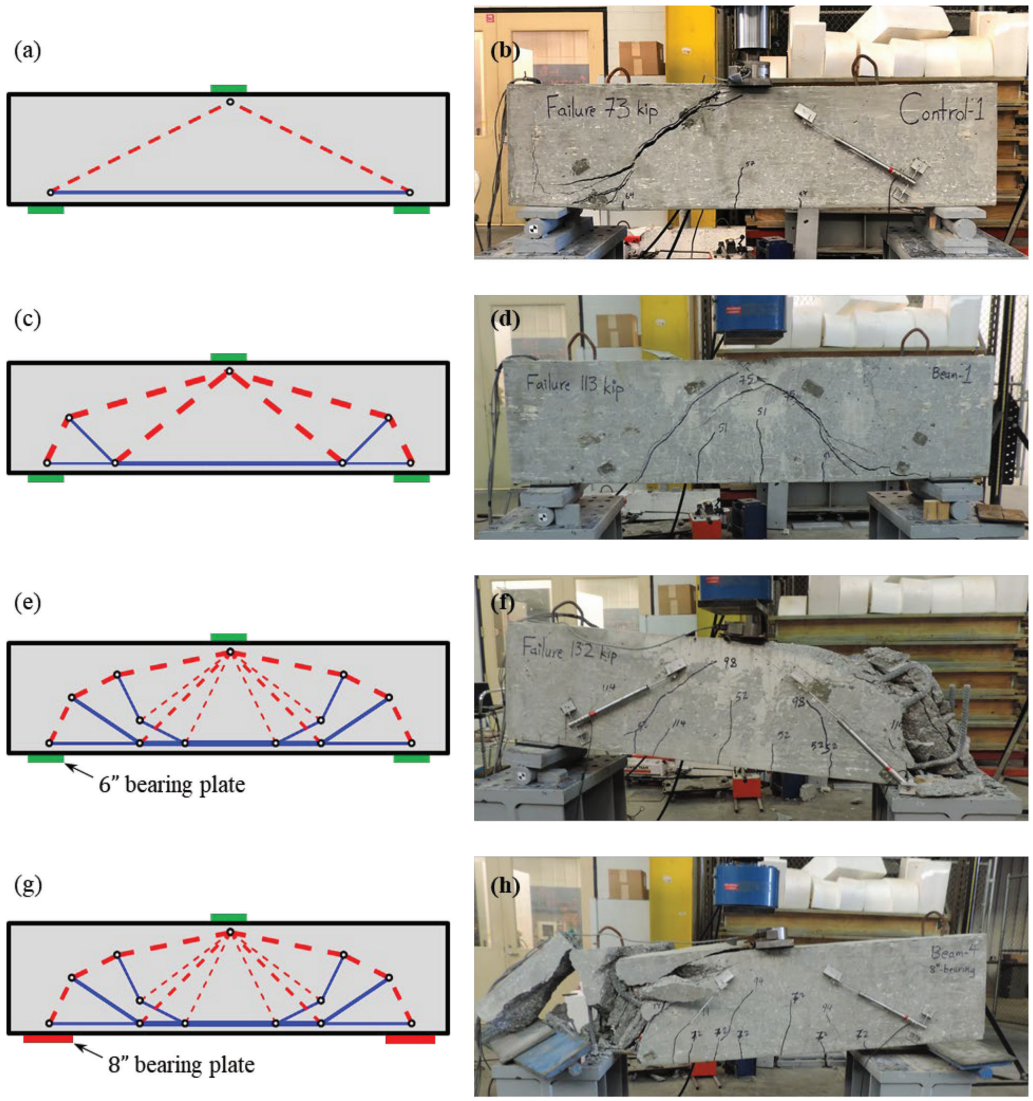

Fig. 11—Failure modes of deep beams considering standard ACI layout with 6 in. (0.15 m) bearing plate, optimized layout I with 6 in. bearing plate, optimized layout II with 6 in. bearing plate, and optimized layout II with 8 in. (0.20 m) bearing plate, respectively.

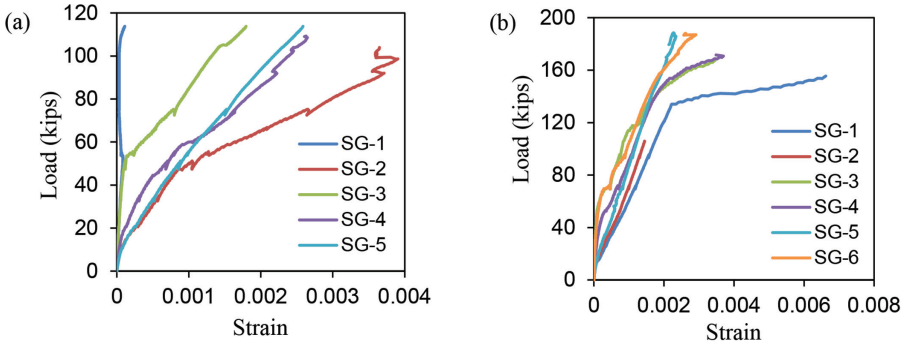

Fig. 12—Strain gauge values with loading for: (a) optimized layout I; and (b) optimized layout II (with 8 in. [0.20 m] bearing plate).

shows the measured strain gauge values of optimized layouts I (Specimen No. 3) and II (Specimen No. 5). As shown in Fig. 12(a), for optimized layout I, yielding was attained in the central region of the reinforcing bars (SG-2, 4, and 5), while SG-1 did not exhibit significant strain in the reinforcing bar because it was near the support. However, for the case of SG-3, it is interesting to note the sudden increase in strain values after the first tension crack and the increasing strain to eventual yielding with the progression of the strut crack. Figure 12(b) presents the load-strain behavior for optimized layout II with an 8 in. (0.20 m) bearing plate. Some key observations can be summarized as follows:

1. SG-1 and SG-5 located in the middle region demonstrated different behaviors due to the shape of the steel reinforcing bars they are attached to. Note that any gauges that appeared to fail early in the loading process are omitted from the reporting of data.

2. SG-3 and SG-4 were attached to the same steel reinforcing bar at two different inclinations; the steel in these regions has yielded, indicating that the inclined regions of the steel reinforcing bar participated in resisting transverse loading in the strut.

3. SG-6 behaved similarly to SG-3 and SG-4 but was on a different reinforcing bar, indicating similar behavior among all inclined reinforcing bars for optimized layout II.

EVALUATION OF STM USING ACI 318 DESIGN CONCEPTS

Table 1 gives the ultimate experimental load attained for each specimen tested. As noted, the beams reinforced with optimized layout II (Specimens No. 4 and 5) supported a larger applied load than the others. In addition, the controlling failure mode of the optimized II design shifted from compression to bearing; a more robust bearing detail would be expected to result in an even greater ultimate load for a beam with optimized layout II. Thus, as expected, the STM layout has a substantial impact on the load-deflection behavior of deep beams. To provide a basis for comparison between the various beam layouts, the ultimate experimental loads are compared to a novel analysis procedure inspired by design guidelines in ACI 318-19. However, it is important to note that the analysis presented herein does not directly follow the ACI design procedures (for optimized layouts). Rather, the analysis procedure is intended to give an insight into the effect of these layouts on the stress fields of the deep beams tested herein. The failure modes checked are the capacity of the nodes, the capacity of the ties, and the capacity of the struts. Based on the failure modes observed in the testing, it has been assumed that the nominal strength of the strut controls the ultimate load of the beam for all layouts to simplify the comparison.

A sketch of the STMs with the standard ACI layout, optimized layout I, and optimized layout II visualizing the force flow in the beam are shown in Fig. 13(a) to (c), respectively. The dashed lines, solid lines, and dimensionless round circles represent the compression elements, tension elements, and nodes (that is, the intersection of struts and ties), respectively. The results of static analysis including the relative internal force magnitudes for the ACI layout, optimized layout I, and optimized layout II are shown in Table 2. This table also summarizes the assumed reinforcement inclination angles for each of the three layouts.

For all the beams, the concrete compressive strength f_c' = 8.5 ksi (58.6 MPa), and the dimensions of the beams are as follows:

- Length of the truss L = 60 in. (1.52 m)
- Height of the truss H = 15 in. (0.38 m)
- Width of the beam b_w = 9 in. (0.23 m)
- Width of the bearing plates $b_1 = b_2$ = 6.0 in. (0.15 m) (Note that Specimen No. 5 with optimized layout II has a different bearing plate at the supports—that is, b_1 = 8 in. [0.2 m].)
- Effective height of the tie w_{T1} = 4 in. (0.1 m)
- Effective height of the node at the applied load w_{T2} = 2 in. (0.05 m)

Standard ACI layout

For the standard ACI STM layout, the standard ACI analysis procedure is followed in a backward fashion in which the load is known and β_s (the strut coefficient) is determined by calibrating the experimental results (that is, the stress in the compression strut at the ultimate load) from testing to the analytical capacity of the strut in compression.

First, calculate the width of the strut at Nodes 1 and 2 using Eq. (10) and (11), and then take the lowest value corresponding to the highest stress (in this case, w_c^2).

$$w_c^1 = b_1 \sin\alpha_1 + w_{T1} \cos\alpha_1 = 6.26 \text{ in. (0.16 m)} \quad (10)$$

$$w_c^2 = (b_2/2)\sin\alpha_1 + w_{T2}\cos\alpha_1 = 3.13 \text{ in. } (0.08 \text{ m}) \quad (11)$$

Then, determine the compressive force in the strut from the known ultimate load $P = 71.1$ kip (316 kN), which is the average of Specimens No. 1 and 2 (refer to Table 1)

$$C_{2n} = 1.118P = 1.118 \times 71.1 \text{ kip } (316 \text{ kN}) = 79.5 \text{ kip } (354 \text{ kN}) \quad (12)$$

The next step is the calculation of the effective compressive stress in the strut at Node 2 using Eq. (13)

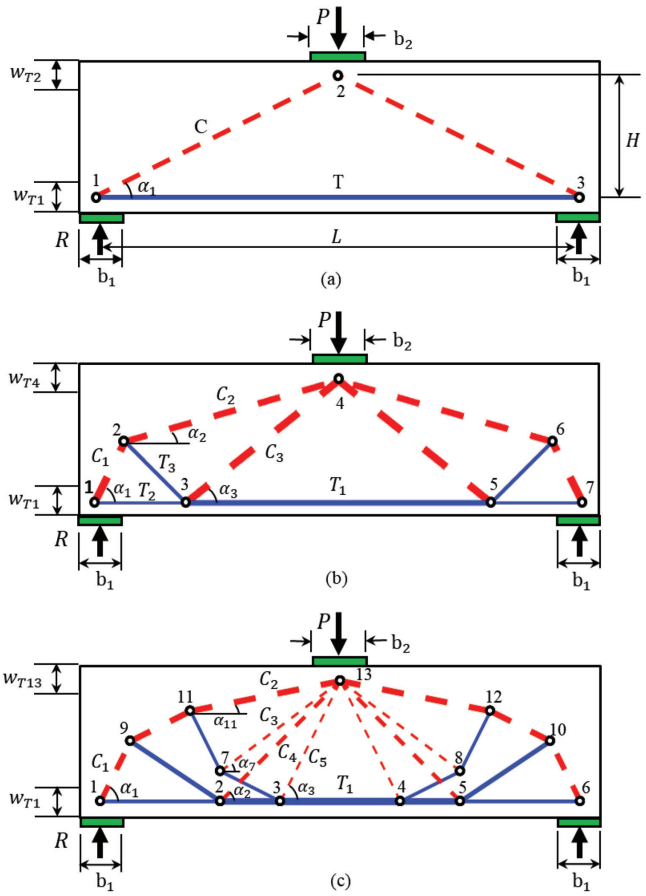

Fig. 13—Deep beam strut-and-tie models: (a) standard ACI STM layout; (b) optimized STM layout I; and (c) optimized STM layout II.

$$f_{ce}^s = \frac{C_{2n}}{w_c^2 b_w} = 2.82 \text{ ksi } (19.4 \text{ MPa}) \quad (13)$$

Using Eq. (14), the value of β_s is obtained, assuming that the strut and node confinement modification factor is equal to 1.0 ($\beta_c = 1.0$)

$$\beta_s = \frac{f_{ce}^s}{0.85\beta_c f_c'} = 0.39 \quad (14)$$

It is noteworthy that this value is very similar to the value found in ACI 318-19 ($\beta_s = 0.4$) for the case of no minimum reinforcement for crack control. The omission of minimum reinforcement was intended to allow a better evaluation of the performance of the novel layouts on the overall performance of the deep beams relative to one another. For this reason, significant transverse cracks were observed.

Optimized layout I

For optimized layout I, the analysis procedure is the same as that given in the previous section, except that the resultant of the forces (C_R) acting at Node 4 (refer to Fig. 13(b)) and the corresponding α_R are calculated with Eq. (15) and (16), respectively. This resolution of forces is intended to simplify the analytical procedure.

$$C_R = \sqrt{(C_2\sin\alpha_2 + C_3\sin\alpha_3)^2 + (C_2\cos\alpha_2 + C_3\cos\alpha_3)^2} = 1.118P \quad (15)$$

$$\alpha_R = \tan^{-1}\left(\frac{C_2\sin\alpha_2 + C_3\sin\alpha_3}{C_2\cos\alpha_2 + C_3\cos\alpha_3}\right) = 0.464 \quad (16)$$

Then, the width of the strut at Nodes 1 and 4 is calculated as

$$w_c^1 = b_1\sin\alpha_1 + w_{T1}\cos\alpha_1 = 7.16 \text{ in. } (0.18 \text{ m}) \quad (17)$$

$$w_c^4 = (b_2/2)\sin\alpha_R + w_{T2}\cos\alpha_R = 3.13 \text{ in. } (0.08 \text{ m}) \quad (18)$$

As $w_c^4 < w_c^1$, then w_c^4 is used for the calculation of the effective compressive stress in the strut at Node 4. Given the ultimate load $P = 114$ kip (507 kN) reached during the

Table 2—Relative magnitudes of internal forces (as fraction of applied load *P*) and angles (in radians) for ACI layout, optimized layout I, and optimized layout II, as shown in Fig. 13(a) to (c), respectively

ACI	T		C		α_1	
	1		1.118		$\tan^{-1}(1/2)$	
Optimized I	T_1	T_2	T_3	C_1	C_2	C_3
	1	0.2500	0.4714	0.5590	0.6067	0.5336
	α_1		α_2		α_3	
	$\tan^{-1}(2)$		$\tan^{-1}(2/7)$		$\tan^{-1}(4/5)$	
Optimized II	T_1	C_1	C_2	C_3	C_4	C_5
	1	0.5590	0.6622	0.1169	0.3030	0.0958
	α_1	α_2	α_3	α_7	α_{11}	
	$\tan^{-1}(2)$	$\tan^{-1}(1)$	$\tan^{-1}(2)$	$\tan^{-1}(3/4)$	$\tan^{-1}(1/5)$	

corresponding experimental test (refer to Table 1), the effective compressive stress is obtained as

$$f_{ce}^{s} = \frac{C_R}{w_c^4 b_w} = \frac{1.118P}{w_c^4 b_w} = 4.52 \text{ ksi (31.2 MPa)} \quad (19)$$

In turn, the value of β_s is calculated, assuming that the strut and node confinement modification factor is equal to 1.0 ($\beta_c = 1.0$)

$$\beta_s = \frac{f_{ce}^{s}}{0.85\beta_c f_c'} = 0.625 \quad (20)$$

The larger value of $\beta_s = 0.625$ calculated for optimized layout I compared to that calculated for the standard ACI layout indicates a more efficient load path in the optimized layout. It should be noted that the β_s value calculated for optimized layout I is less than the value $\beta_s = 0.75$, which assumes the inclusion of minimum distributed reinforcement for crack control.

Optimized layout II

Similar to the procedure shown in the previous section, the resultant of the forces acting at Node 13 (refer to Fig. 13(c)) is determined (C_R) for optimized layout II with its corresponding α_R as shown in Eq. (21) and (22).

$$\begin{aligned} C_{Rx} &= C_2\sin\alpha_{11} + C_3\sin\alpha_7 + C_4\sin\alpha_2 + C_5\sin\alpha_3 = 0.5P \\ C_{Ry} &= C_2\cos\alpha_{11} + C_3\cos\alpha_7 + C_4\cos\alpha_2 + C_5\cos\alpha_3 = P \end{aligned} \quad (21)$$

$$\begin{aligned} C_R &= \sqrt{(C_{Rx})^2 + (C_{Ry})^2} = 1.118P \\ \alpha_R &= \tan^{-1}\left(\frac{C_{Rx}}{C_{Ry}}\right) = 0.464 \end{aligned} \quad (22)$$

For the optimized layout II with a 6 in. bearing plate (that is, $b_1 = 6$ in. [0.15 m]), the width of the strut at Nodes 1 and 13 is calculated as

$$w_c^1 = b_1\sin\alpha_1 + w_{T1}\cos\alpha_1 = 7.16 \text{ in. (0.18 m)} \quad (23)$$

$$w_c^{13} = (b_2/2)\sin\alpha_R + w_{T2}\cos\alpha_R = 3.13 \text{ in. (0.08 m)} \quad (24)$$

where the smaller value w_c^{13} is selected for calculating the effective compressive stress in the strut at Node 13. It is also known that the ultimate load $P = 131$ kip (583 kN) from the experiment (refer to Table 1). Following the same procedure presented in the previous section, the value of β_s is calculated, assuming that the strut and node confinement modification factor is equal to 1.0 ($\beta_c = 1.0$)

$$\beta_s = \frac{f_{ce}^{s}}{0.85\beta_c f_c'} = \left(\frac{C_R}{w_c^{13} b_w}\right)/(0.85\beta_c f_c') = \left(\frac{1.118P}{w_c^{13} b_w}\right)/(0.85\beta_c f_c') = 0.719 \quad (25)$$

For the optimized layout II with an 8 in. bearing plate (that is, $b_1 = 8$ in. [0.2 m]), the width of the strut at Nodes 1 and 13 is obtained as

$$w_c^1 = b_1\sin\alpha_1 + w_{T1}\cos\alpha_1 = 8.94 \text{ in. (0.23 m)} \quad (26)$$

$$w_c^{13} = (b_2/2)\sin\alpha_R + w_{T2}\cos\alpha_R = 3.13 \text{ in. (0.08 m)} \quad (27)$$

Given the ultimate load $P = 189$ kip (841 kN) from the experiment (refer to Table 1), the value of β_s is obtained, assuming that the strut and node confinement modification factor is equal to 1.0 ($\beta_c = 1.0$)

$$\beta_s = \left(\frac{1.118P}{w_c^{13} b_w}\right)/(0.85\beta_c f_c') = 1.038 \quad (28)$$

All the results are summarized in Table 3. The resulting β_s for the optimized layout II with a 6 in. (0.15 m) bearing plate (Specimen No. 4) shows a slightly improved performance because of the premature bearing failure, but with even more improvement in the ultimate load. However, β_s for optimized layout II with an 8 in. (0.20 m) bearing plate (Specimen No. 5) shows that a more desirable load path is used when premature bearing failure is suppressed. It is important to note that the calculations for both optimized layout II with 6 and 8 in. (0.15 and 0.20 m) bearing plates are based on the assumption that the nominal strength of the strut controls the ultimate failure. Nonetheless, for the specific case of optimized layout II, a bearing failure was observed rather than a strut failure, so the actual values of β_s will be higher than the calculated value herein.

CONCLUSIONS

This work presents a multi-material/multi-volume topology optimization framework to design practical strut-and-tie model (STM) layouts for reinforced concrete (RC) structures. Inspired by Michell's optimality conditions, the efficiency of optimized STM layouts is quantified by the load path Z (or the Michell number), which serves as a simple and efficient criterion for evaluating any STM. An experimental testing program indicated that the optimized STM layouts possess significantly improved behavior compared to the traditional layout using the same overall reinforcement ratio. As such, it is expected that designs with optimized layouts could result in smaller total volume of reinforcing steel needed to resist a given set of design loads, resulting in a more economical design. It is acknowledged that, at present, the more complex reinforcement layouts may increase fabrication costs. However, given advancements in reinforcement layout construction using computer-aided reinforcement fabrication, it is anticipated that reducing the total volume of steel needed in a given deep beam design will eventually

Table 3—Summary of analysis results for all layouts (refer to Fig. 13 for node numbering)

Standard ACI layout	w_c^1	w_c^2	C_{2n}	f_{ce}^s	β_s
	6.26 in. (0.16 m)	3.13 in. (0.08 m)	79.5 kip (354 kN)	2.82 ksi (19.4 MPa)	0.390
Optimized layout I	w_c^1	w_c^4	C_R (equal to C_{4n})	f_{ce}^s	β_s
	7.16 in. (0.18 m)	3.13 in. (0.08 m)	128 kip (569 kN)	4.52 ksi (35.2 MPa)	0.625
Optimized layout II with 6 in. bearing plate	w_c^1	w_c^{13}	C_R (equal to C_{13n})	f_{ce}^s	β_s
	7.16 in. (0.18 m)	3.13 in. (0.08 m)	146 kip (649 kN)	5.20 ksi (35.9 MPa)	0.719
Optimized layout II with 8 in. bearing plate	w_c^1	w_c^{13}	C_R (equal to C_{13n})	f_{ce}^s	β_s
	8.94 in. (0.23 m)	3.13 in. (0.08 m)	211 kip (939 kN)	7.49 ksi (51.6 MPa)	1.038

Note: 1.0 in. = 25.4 mm; 1.0 kip = 4.45 kN; 1.0 ksi = 6.89 MPa.

result in a more efficient and cost-effective design. Given the significantly reduced cracking observed in the optimized layouts compared to the traditional STM layout, it is possible that the optimized layouts would require less crack-control reinforcement, potentially further reducing the total volume of steel needed in the deep beams.

In addition, to extend the present framework as a practical RC structures design tool, further research could be conducted in the following aspects: 1) a three-dimensional (3-D) design domain with a complex stress state; 2) incorporating realistic plasticity material models in the optimization framework for concrete and steel; 3) achieving higher structural ductility through transverse reinforcement optimization; and 4) the application of the design and analysis procedures presented herein to a database of known reliable experimental results for deep beams available in the established literature.

ACKNOWLEDGMENTS

The authors acknowledge the support from the U.S. National Science Foundation (NSF) under grant No. 2105811.

AUTHOR BIOS

Tuo Zhao *is a Postdoctoral Research Associate in the Department of Civil and Environmental Engineering at Princeton University, Princeton, NJ. He was the winner of the ACI Georgia Chapter LaGrit F. "Sam" Morris Student Scholarship. His research interests include multi-material topology optimization and nonlinear analysis of reinforced concrete (RC) structures.*

Ammar A. Alshannaq *is an Assistant Professor in the Department of Civil Engineering at Yarmouk University, Irbid, Jordan. His research interests include repairing and strengthening existing RC structures, characterization and testing of fiber-reinforced polymer (FRP) materials, and optimization and novel design of deep RC beams.*

David W. Scott *is a Professor in the Department of Civil Engineering and Construction at Georgia Southern University, Statesboro, GA. He is a member of ACI Committees E706, Concrete Repair Education; 364, Rehabilitation; 440, Fiber-Reinforced Polymer Reinforcement; and 546, Repair of Concrete. His research interests include novel materials and systems for civil infrastructure, evaluation of highway safety structures, and repair of concrete structures.*

Glaucio H. Paulino *is the Margareta Engman Augustine Professor at Princeton University. He is a Professor of the Civil and Environmental Engineering Department, and the Princeton Materials Institute (PMI). His research interests include the development of methodologies to characterize the deformation and fracture behavior of existing and emerging materials and structural systems, and topology optimization for multiscale/multiphysics problems.*

REFERENCES

ACI Committee 318, 2019, "Building Code Requirements for Structural Concrete (ACI 318-19) and Commentary (ACI 318R-19) (Reapproved 2022)," American Concrete Institute, Farmington Hills, MI, 624 pp.

Birrcher, D.; Tuchscherer, R.; Huizinga, M.; Bayrak, O.; Wood, S.; and Jirsa, J., 2009, "Strength and Serviceability Design of Reinforced Concrete Deep Beams," Report No. FHWA/TX-09/0-5253-1, Center for Transportation Research, The University of Texas at Austin, Austin, TX, 400 pp.

Breña, S. F., and Roy, N. C., 2009, "Evaluation of Load Transfer and Strut Strength of Deep Beams with Short Longitudinal Bar Anchorages," *ACI Structural Journal*, V. 106, No. 5, Sept.-Oct., pp. 678-689.

Bruggi, M., 2010, "On the Automatic Generation of Strut and Tie Patterns under Multiple Load Cases with Application to the Aseismic Design of Concrete Structures," *Advances in Structural Engineering*, V. 13, No. 6, Dec., pp. 1167-1181. doi: 10.1260/1369-4332.13.6.1167

Christensen, P. W., and Klarbring, A., 2008, *An Introduction to Structural Optimization*, Springer Science+Business Media B.V., Dordrecht, the Netherlands.

Dorn, W. S.; Gomory, R. E.; and Greenberg, H. J., 1964, "Automatic Design of Optimal Structures," *Journal de Mécanique*, V. 3, No. 1, pp. 25-52.

Gaynor, A. T.; Guest, J. K.; and Moen, C. D., 2013, "Reinforced Concrete Force Visualization and Design Using Bilinear Truss-Continuum Topology Optimization," *Journal of Structural Engineering*, ASCE, V. 139, No. 4, Apr., pp. 607-618. doi: 10.1061/(ASCE)ST.1943-541X.0000692

Groenwold, A. A., and Etman, L. F. P., 2008, "On the Equivalence of Optimality Criterion and Sequential Approximate Optimization Methods in the Classical Topology Layout Problem," *International Journal for Numerical Methods in Engineering*, V. 73, No. 3, Jan., pp. 297-316. doi: 10.1002/nme.2071

He, Z.-Q.; Liu, Z.; Wang, J.; and Ma, Z. J., 2020, "Development of Strut-and-Tie Models Using Load Path in Structural Concrete," *Journal of Structural Engineering*, ASCE, V. 146, No. 5, May, p. 06020004. doi: 10.1061/(ASCE)ST.1943-541X.0002631

Ismail, K. S., 2016, "Shear Behaviour of Reinforced Concrete Deep Beams," PhD thesis, University of Sheffield, Sheffield, UK, 312 pp.

Ismail, K. S.; Guadagnini, M.; and Pilakoutas, K., 2018, "Strut-and-Tie Modeling of Reinforced Concrete Deep Beams," *Journal of Structural Engineering*, ASCE, V. 144, No. 2, Feb., p. 04017216. doi: 10.1061/(ASCE)ST.1943-541X.0001974

Jewett, J. L., and Carstensen, J. V., 2019, "Experimental Investigation of Strut-and-Tie Layouts in Deep RC Beams Designed with Hybrid Bi-linear Topology Optimization," *Engineering Structures*, V. 197, Oct., Article No. 109322. doi: 10.1016/j.engstruct.2019.109322

Kondalraj, R., and Appa Rao, G., 2021, "Experimental Verification of ACI 318 Strut-and-Tie Method for Design of Deep Beams without Web Reinforcement," *ACI Structural Journal*, V. 118, No. 1, Jan., pp. 139-152.

Kumar, P., 1978, "Optimal Force Transmission in Reinforced Concrete Deep Beams," *Computers & Structures*, V. 8, No. 2, Apr., pp. 223-229. doi: 10.1016/0045-7949(78)90026-3

Leu, L.-J.; Huang, C.-W.; Chen, C.-S.; and Liao, Y.-P., 2006, "Strut-and-Tie Design Methodology for Three-Dimensional Reinforced Concrete Structures," *Journal of Structural Engineering*, ASCE, V. 132, No. 6, June, pp. 929-938. doi: 10.1061/(ASCE)0733-9445(2006)132:6(929)

Liang, Q. Q.; Xie, Y. M.; and Steven, G. P., 2000, "Topology Optimization of Strut-and-Tie Models in Reinforced Concrete Structures Using an

Evolutionary Procedure," *ACI Structural Journal*, V. 97, No. 2, Mar.-Apr., pp. 322-331.

Liang, Q. Q.; Xie, Y. M.; and Steven, G. P., 2001, "Generating Optimal Strut-and-Tie Models in Prestressed Concrete Beams by Performance-Based Optimization," *ACI Structural Journal*, V. 98, No. 2, Mar.-Apr., pp. 226-232.

MacGregor, J. G., 1997, *Reinforced Concrete: Mechanics and Design*, Prentice Hall, Upper Saddle River, NJ.

Martinez, G. A.; Beiter, K. S.; Ghiami Azad, A. R.; Polo, G. E.; Shinn, R. L.; Hrynyk, T. D.; and Bayrak, O., 2017, "Testing and Analysis of Two Deep Beams Designed Using Strut-and-Tie Method," *ACI Structural Journal*, V. 114, No. 6, Nov.-Dec., pp. 1531-1542. doi: 10.14359/51689504

Maxwell, J. C., 1864, "XLV. On Reciprocal Figures and Diagrams of Forces," *The London, Edinburgh, and Dublin Philosophical Magazine and Journal of Science*, V. 27, No. 182, Series 4, pp. 250-261. doi: 10.1080/14786446408643663

Michell, A. G. M., 1904, "LVIII. The Limits of Economy of Material in Frame-Structures," *The London, Edinburgh, and Dublin Philosophical Magazine and Journal of Science*, V. 8, No. 47, Series 6, pp. 589-597. doi: 10.1080/14786440409463229

Mozaffari, S.; Akbarzadeh, M.; and Vogel, T., 2020, "Graphic Statics in a Continuum: Strut-and-Tie Models for Reinforced Concrete," *Computers & Structures*, V. 240, Nov., Article No. 106335. doi: 10.1016/j.compstruc.2020.106335

Panjehpour, M.; Chai, H. K.; and Voo, Y. L., 2015, "Refinement of Strut-and-Tie Model for Reinforced Concrete Deep Beams," *PLOS ONE*, V. 10, No. 6, June, Article No. e0130734. doi: 10.1371/journal.pone.0130734

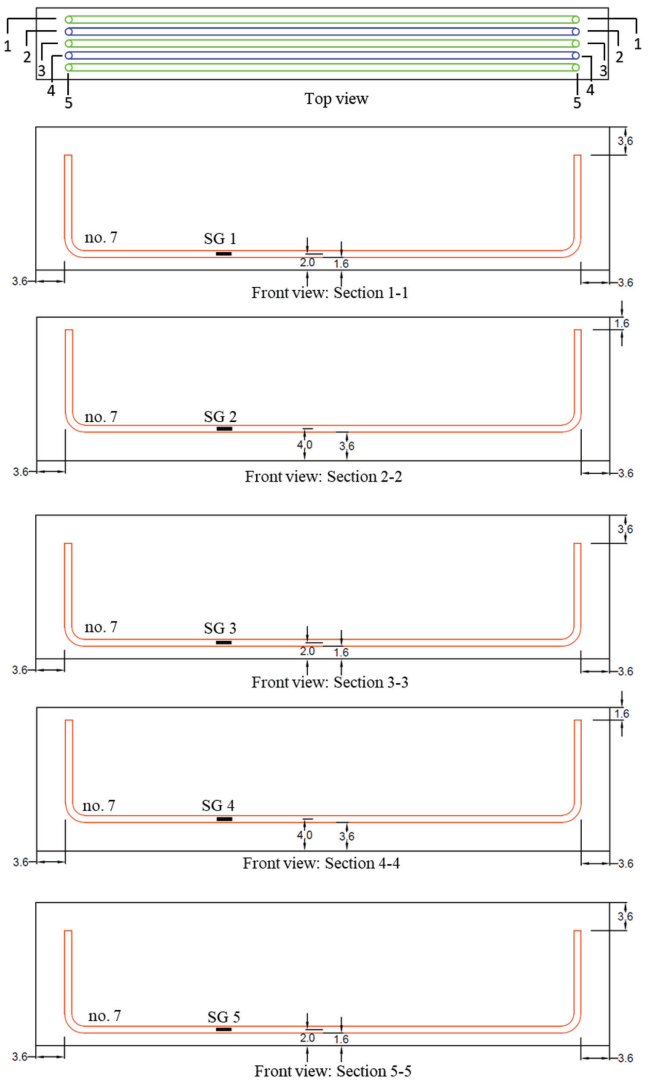

Fig. A1—Reinforcement details of specimen with standard ACI STM layout. (Note: Labeled dimensions are in inches; 1.0 in. = 25.4 mm.)

Rezaei, N.; Klein, G.; and Garber, D. B., 2019, "Strut Strength and Failure in Full-Scale Concrete Deep Beams," *ACI Structural Journal*, V. 116, No. 3, May, pp. 65-74. doi: 10.14359/51713306

Sanders, E. D.; Aguiló, M. A.; and Paulino, G. H., 2018, "Multi-Material Continuum Topology Optimization with Arbitrary Volume and Mass Constraints," *Computer Methods in Applied Mechanics and Engineering*, V. 340, Oct., pp. 798-823. doi: 10.1016/j.cma.2018.01.032

Sanders, E. D.; Ramos, A. S. Jr.; and Paulino, G. H., 2020, "Topology Optimization of Tension-Only Cable Nets under Finite Deformations," *Structural and Multidisciplinary Optimization*, V. 62, No. 2, Aug., pp. 559-579. doi: 10.1007/s00158-020-02513-7

Schlaich, J.; Schäfer, K.; and Jennewein, M., 1987, "Toward a Consistent Design of Structural Concrete," *PCI Journal*, V. 32, No. 3, May-June, pp. 74-150. doi: 10.15554/pcij.05011987.74.150

Victoria, M.; Querin, O. M.; and Martí, P., 2011, "Generation of Strut-and-Tie Models by Topology Design Using Different Material Properties in Tension and Compression," *Structural and Multidisciplinary Optimization*, V. 44, No. 2, Aug., pp. 247-258. doi: 10.1007/s00158-011-0633-z

Xia, Y.; Langelaar, M.; and Hendriks, M. A. N., 2020, "A Critical Evaluation of Topology Optimization Results for Strut-and-Tie Modeling of Reinforced Concrete," *Computer-Aided Civil and Infrastructure Engineering*, V. 35, No. 8, Aug., pp. 850-869. doi: 10.1111/mice.12537

Zhang, X. S.; Paulino, G. H.; and Ramos, A. S. Jr., 2018, "Multi-Material Topology Optimization with Multiple Volume Constraints: A General Approach Applied to Ground Structures with Material Nonlinearity," *Structural and Multidisciplinary Optimization*, V. 57, No. 1, Jan., pp. 161-182. doi: 10.1007/s00158-017-1768-3

Zhou, L., and Wan, S., 2021, "Development of Strut-and-Tie Models Using Topology Optimization Based on Modified Optimal Criterion," *Structural Concrete*, V. 22, No. 6, Dec., pp. 3304-3314. doi: 10.1002/suco.202100123

APPENDIX A

This Appendix details the reinforcement design including the location of strain gauges for the standard ACI STM layout (Fig. A1), optimized layout I (Fig. A2), and optimized layout II (Fig. A3), respectively.

APPENDIX B

Appendix B includes an example to show the calculation of the Michell number Z for the STM layout in Fig. 3(d). Because this truss system is statically determinate, the internal axial force of the members can be calculated using the equilibrium conditions—that is, $N_{12} = N_{67} = -0.56P$, $N_{24} = N_{46} = -0.61P$, $N_{34} = N_{45} = -0.53P$, $N_{13} = N_{57} = 0.25P$, $N_{23} = N_{56} = 0.47P$, and $N_{35} = P$ (refer to the labeled node numbers in Fig. B1). Moreover, the length of each truss member is given as $L_{12} = L_{67} = 0.56H$, $L_{24} = L_{46} = 1.82H$, $L_{34} = L_{45} = 1.6H$, $L_{13} = L_{57} = 0.75H$, $L_{23} = L_{56} = 0.71H$, and $L_{35} = 2.5H$. Therefore, the Michell number Z can be obtained using Eq. (1) as $Z = \Sigma_e|F_e|L_e = 2|F_{12}|L_{12} + 2|F_{24}|L_{24} + 2|F_{34}|L_{34} + 2|F_{13}|L_{13} + 2|F_{23}|L_{23} + F_{35}|L_{35} = 8.08PH$.

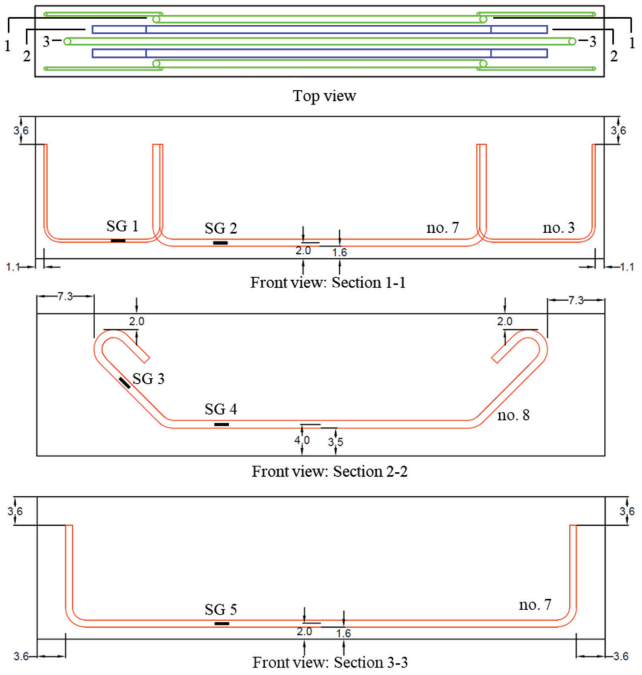

Fig. A2—Reinforcement details of specimen with the optimized STM layout I. (Note: Labeled dimensions are in inches; 1.0 in. = 25.4 mm.)

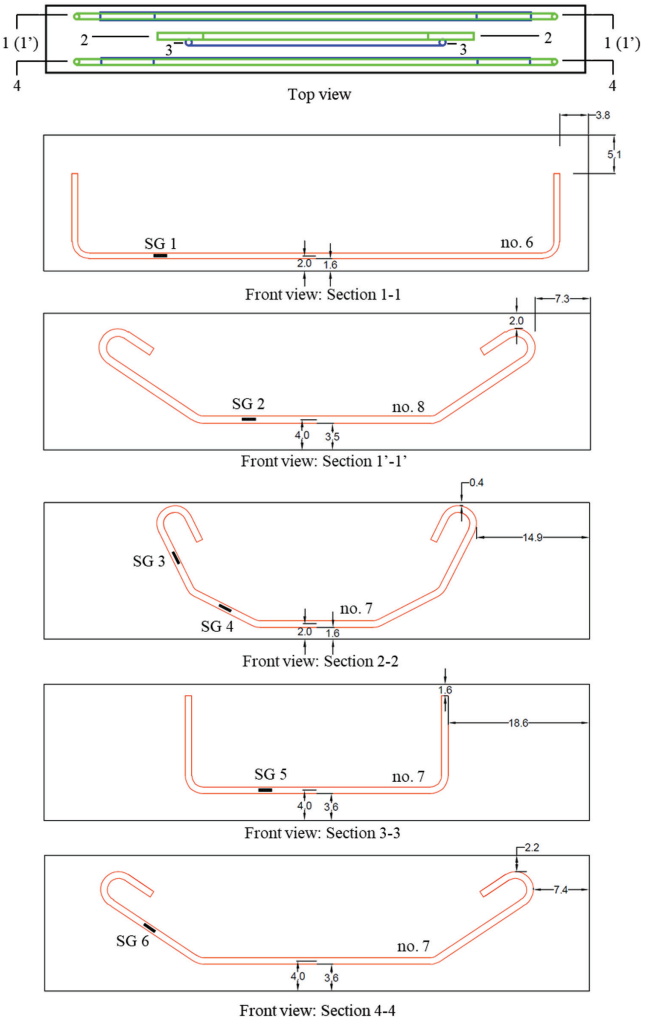

Fig. A3—Reinforcement details of specimen with optimized STM layout II. (Note: Labeled dimensions are in inches; 1.0 in. = 25.4 mm.)

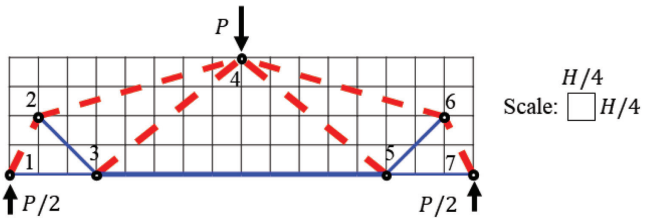

Fig. B1—Labeled node numbers for truss system in Fig. 3(d).

ACI STRUCTURAL JOURNAL

The American Concrete Institute (ACI) is a leading authority and resource worldwide for the development and distribution of consensus-based standards and technical resources, educational programs, and certifications for individuals and organizations involved in concrete design, construction, and materials, who share a commitment to pursuing the best use of concrete.

Individuals interested in the activities of ACI are encouraged to explore the ACI website for membership opportunities, committee activities, and a wide variety of concrete resources. As a volunteer member-driven organization, ACI invites partnerships and welcomes all concrete professionals who wish to be part of a respected, connected, social group that provides an opportunity for professional growth, networking, and enjoyment.

American Concrete Institute